ingegneria sismica
International Journal of Earthquake Engineering
Anno XLIII - Num. 2 - 2026

Research on Temperature Field Prediction and Optimization Methods in Energy Saving Design of Buildings Based on IDW Algorithm

Han Yan[1], *Huanzhen Gao*[1], *Xiaodong Ding*[1,*] *and Xijian Liang*[2]

[1] Department of New Materials and Architectural Engineering, Zaozhuang Vocational College, Zaozhuang, Shandong, 277800, China
[2] Shandong Xinzhizhu Information Technology Co., Ltd., Jinan, Shandong, 250101, China

SUMMARY: *Reducing the waste of building energy is important for the development of green environment. In this paper, based on the dynamic calculation method of various types of cold loads in the building temperature field, a four-wire platinum RTD sensor is selected as the physical device for real-time monitoring of space temperature to improve the credibility of temperature collection. The inverse distance weight model based on local parameter optimization is constructed, combined with particle swarm optimization algorithm and K-dimensional tree, etc., to realize temperature field prediction and energy consumption optimization. The constructed model is applied to the temperature prediction simulation and energy saving optimization practice of large buildings to judge the practical value of the model. The results show that the data collection error is minimized when the search height distance is 2 and the weight coefficient is 2.5-3. In the comparison between the model simulation prediction value and the measured temperature value, the average value of temperature difference in the horizontal and vertical directions is 0.250℃ and 0.162℃ respectively, which is a small error. In 10 energy consumption optimization experiments, this paper's model is able to achieve the optimization of building energy consumption of 0.08-0.80kWh/m². Using the model of this paper can carry out high-precision prediction and energy consumption optimization of building energy-saving design.*

KEYWORDS: *cold load calculation; temperature field prediction; inverse distance weight model; particle swarm algorithm; building energy efficiency*

1 Introduction

With the increasing global energy consumption and environmental problems, energy efficiency in buildings has become an important topic [1, 2]. Energy efficiency is one of the crucial factors when designing buildings [3]. Building energy-saving design is to ensure the improvement of building comfort under the condition of rational use of energy and constantly improve the efficiency of energy utilization [4, 5]. Building energy-saving design is a more complex systematic project, which, as an important area in which people's production and life are inextricably linked, must be designed from the actual situation of building energy-saving design in the process of designing, and on the basis of ensuring the normal use of the building's function and quality, to take a variety of effective methods to carry out energy-saving planning and design of the building [6-9].

In the process of building design, designers need to consider many factors, among which

*zzvcdxd@163.com
https://doi.org/10.65102/is2026504 Published: 30 April, 2026

the temperature field is a key link, especially in the region of high temperature in summer and low temperature in winter [10, 11]. Therefore, it is very necessary to predict and optimize the temperature field in building design, which can be beneficial to the design and construction of the building, as well as later use and maintenance, and help designers to optimize the thermal environment parameters of the building in order to meet the needs of different user groups, and minimize energy loss and unnecessary consumption [12-15].

This paper integrates building temperature field cold load refinement calculation, four-wire platinum RTD sensing network temperature acquisition, and anisotropic inverse distance weight model to achieve accurate prediction of building temperature field and dynamic optimization of energy consumption. Ensure the accuracy of cold load calculation by analyzing the cold load calculation method of each type of temperature field. Design contact temperature sensor to realize the measurement accuracy of multi-type temperature data collection. Utilize particle swarm algorithm and so on to realize the local optimization of parameters and solve the limitation of traditional inverse distance weighting method. Using the constructed model, analyze the relationship between the search distance and the weight coefficients, and determine the optimal parameter with the smallest error. Mining the temperature difference characteristics of the selected building in the vertical and horizontal directions through the measured behavior. Compare the differences between the predicted simulated values of the model and the measured values to verify the temperature field prediction effect of the model. Comparative experiments are conducted to demonstrate the advantages of the model in this paper for energy-saving design solutions.

2 Technical support for building temperature field prediction and optimization

In this chapter, the related technology is elaborated from three dimensions: building temperature field cold load calculation, hardware design of real-time monitoring and visualization system for spatial temperature distribution, and construction of inverse distance weighting model.

2.1 Calculation of building temperature field cold loads

2.1.1 Calculation of building envelope cold loads

Enclosure refers to the walls, doors, windows, roofs, floors, etc. that surround the building space, constituting the building space and resisting the unfavorable effects of the environment (also including certain accessories). According to whether the enclosure structure is in direct contact with the outside air, it can be categorized into external enclosure structure and internal enclosure structure. The external enclosure structure includes external walls, roofs, side windows, external doors, etc., which are used to resist wind and rain, temperature changes, solar radiation, etc., and should have the characteristics of heat insulation, thermal insulation, acoustic insulation, moisture-proofing, waterproofing, fire-resistance and durability. Partition wall, floor, doors and windows and other internal enclosure structure, play a role in separating the indoor space, should have sound insulation, isolation of the line of sight, as well as some special requirements of the performance.

The summer cold load of the building envelope accounts for a high proportion of the total cold load, and the cold load of the envelope accounts for about 75% of the total cold load in residential buildings, and the proportion is lower in public buildings. In the energy consumption of building envelope, external windows (including transparent curtain walls and balcony doors) are the worst thermal performance components among the three major envelope components of

roofs, walls and external windows, and they are one of the most important factors affecting the quality of the indoor thermal environment and the energy consumption of buildings. At present, in China's public buildings, the energy consumption of windows is about 3.5 times that of walls and 4.5 times that of roofs, accounting for about 45%-55% of the total energy consumption of the building envelope.

1) Heat and cold load of glass windows

The formula for calculating the heat transfer and cold load of glass windows is as follows:

$$Q_2 = x_k K_c F_c \left(t_{wp} + \Delta t_k - t_n \right) \tag{1}$$

where Q_2 - the cold load of heat transfer from the glass window (W);

x_k - correction coefficient of heat transfer coefficient of glass window;

K_c - heat transfer coefficient of glass window (W/(m²-°C));

F_c - area of the window including the window frame (m²);

t_{wp} - calculated average daily temperature outside the air-conditioned room in summer (°C);

Δt_k - hour-by-hour outdoor temperature difference in summer (°C);

t_n - calculated indoor temperature (°C).

(2) Cold load of exterior wall and roof

The formula for calculating the cold load of exterior wall and roof cover is as follows:

$$Q_w = K_w F_w \left(t_{wp} + \Delta t_{fp} + \Delta t_w - t_n \right) \tag{2}$$

$$\Delta t_{fp} = \frac{J_p \rho}{\alpha_w} \tag{3}$$

Eq. (2) where Q_w - the cold load (W) of the roof (or wall) at the “calculation time”;

K_w - heat transfer coefficient of the roof (or wall);

F_w - area of the roof (or wall);

t_{wp} - calculated average daily temperature outside the air-conditioned room in summer (°C);

Δt_{fp} - the average temperature rise of radiation on the external surface of the roof (or external wall) (°C);

Δt_w - the combined load temperature difference (°C) of the “action time” outdoor temperature fluctuation part of the roof (or facade);

t_n - indoor calculated temperature;

Equation (3) in J_p - solar radiation daily average illuminance (W / m²);

ρ - solar radiation absorption coefficient of the external surface of the maintenance structure;

α_w - heat transfer coefficient of the external surface of the maintenance structure.

(3) Cold load of internal walls, internal windows, floor slabs and floors

Internal walls, internal windows, floor and other maintenance structures, when the neighboring room is a non-air-conditioned room, the neighboring room temperature using the average temperature of the neighboring room, the cold load is calculated according to the following formula:

$$Q_4 = KF\left(t_{wp} + \Delta t_{ls} - t_n\right) \tag{4}$$

Q_4 - the cooling load (W) for heat transfer through the internal wall or floor slab;

K - heat transfer coefficient of the internal wall or floor slab;

F - area of the internal wall or floor slab;

Δt_{ls} - the difference between the average temperature of the neighboring room and the average daily temperature calculated outside the air-conditioned room in summer (℃);

The cold load of the ground, comfort air-conditioning room in summer ground cold load can not be calculated, for process air-conditioning room, there is an external wall, only calculate the distance from the wall within 2m of the ground heat transfer as a cold load. That is, the formula:

$$Q_D = K_D F_D\left(t_{wp} - t_n\right) \tag{5}$$

where Q_D - ground cooling load (W);

K_D - ground heat transfer coefficient;

F_D - the ground area within 2m from the outer wall.

2.1.2 Fresh air cooling load calculation

Fresh air system to the outdoor fresh air into the air-conditioning room, summer due to high outdoor temperatures, the imported fresh air temperature does not reach the temperature requirements of the air-conditioning room, will inevitably produce a cold load. The formula for calculating the cold load of fresh air is as follows:

$$Q_N = \left(h_w - h_n\right) \times L\left(1 - \eta\zeta\right) \tag{6}$$

where Q_N - total heat and cold load of fresh air;

h_w - enthalpy value (kJ/kg) when calculating the parameters outside in summer;

h_n - enthalpy of indoor air (kJ/kg);

L - volume of fresh air penetrating deep into the room (m³/h);

η - full heat recovery efficiency (0-1), 0 when there is no heat recovery;

ζ - exhaust air ratio (0-1), i.e., exhaust air volume/fresh air volume of the heat recovery device.

2.1.3 Calculation of outdoor heat, humidity and cold loads

Outdoor heat and humidity parameters mainly include outdoor air temperature, outdoor air humidity, wind speed, wind direction, precipitation, ground temperature and other parameters, which is an important basis for thermal design of buildings. Outdoor heat and humidity parameters are not only in the building design to determine the construction of the building envelope and the choice of material application, affecting the overall arrangement of the building group, the shape of the building and the choice of house orientation, etc., but also the source of air conditioning cold load.

The formula for calculating the infiltration air cooling load is as follows:

$$Q_q = \frac{1}{3.6}\rho_w L\left(h_w - h_n\right) \tag{7}$$

where Q_q - full cooling load (W) for infiltrated air volume;

ρ_w - air density at the calculated dry bulb temperature outside the air-conditioned room in summer;

L - total air volume penetrating into the room (m^3/h);

h_w - enthalpy (kJ/kg) at the calculated parameters outdoors in summer;

h_n - enthalpy of indoor air (kJ/kg).

2.2 Hardware design of real-time monitoring and visualization system for space temperature distribution

2.2.1 Overall system hardware program design

In this design, the system hardware mainly includes the following four parts, sensor module, analog-to-digital conversion (ADC) module, microcontroller module, and wireless transmitting module.

1) Sensor module: this module is responsible for collecting the temperature and converting the collected temperature information into a voltage signal;

2) ADC module: it is responsible for converting the incoming voltage signal in the sensor module into a digital signal, realizing the transformation from analog to digital;

3) Microcontroller module: this module is the brain of the hardware part of the whole system, controlling a series of actions such as acquiring and sending temperature information;

4) Wireless transmission module: responsible for wireless data transmission, the converted temperature signal wireless transmission to the host computer.

2.2.2 Temperature acquisition sensor module circuit design

Temperature sensors commonly used on the market today can be broadly categorized into the following two main types: contact temperature sensors and non-contact temperature sensors. Contact temperature sensors are used to collect temperature information through direct contact with the measured object. This type of temperature sensor is widely used in a variety of temperature measurement occasions because of its lower cost, measurement accuracy and other advantages. Non-contact temperature sensors collect temperature information by measuring the thermal radiation of the object to be measured, and therefore can realize telemetry. This measurement method is theoretically unlimited in temperature measurement range because it is not in direct contact with the measured target. It is also not limited by the heat resistance of the sensor itself. However, the cost of this type of sensor is high and the accuracy is low. Based on the above analysis, this paper mainly uses contact temperature sensors.

For the temperature sensors commonly used in the market can be roughly divided into four categories. By comparing the common temperature sensors, this paper will select the platinum RTD as the temperature sensing element of the system, the system requires the temperature measurement range of -5 ℃ -45 ℃, in the range of platinum RTD has good linearity, and the system requires the measurement accuracy of 0.01 ℃, so the platinum RTD can meet the measurement requirements.

In this paper, platinum RTD PT100 is selected as the temperature sensing element, and firstly, the functional relationship between Pt100 platinum resistance and temperature is briefly introduced, Pt100 has a large temperature measurement range (-205℃-655℃), and the

corresponding resistance value within the range is 20Ω-340Ω. At this time, the expression of the functional relationship between Pt100 and the temperature corresponds to:

$$R_t = \begin{cases} R_0\left(1+At+Bt^2+C\left(t-101\right)t^3\right) & -200 \le t \le 0 \\ R_0\left(1+At+Bt^2\right) & 0 < t < 650 \end{cases} \tag{8}$$

In equation (8): R_t is the resistance value of Pt100 at t℃, where $R_0 = 101$℃, $A = 3.909\times10^{-3}$, $B = -5.78\times10^{-7}$, and $C = -4.184\times10^{-12}$.

From the above relation, we can get the resistance value corresponding to each temperature in a certain temperature range. Based on this, we only need to measure the voltage value in Pt100 which is caused by the change of resistance value and the corresponding voltage change, then we can get the current temperature value. There are three types of wiring for Pt100, which are 2-wire, 3-wire and 4-wire.

1) 2-wire connection. The name of the two-wire system comes from the two ends of the Pt100 are connected to two wires, shown in the figure for L_1, L_2. Through these two wires for the Pt100 to apply the excitation current I, at this time, respectively, measured its two ends of the potential V_1, V_2. And the resistance value of RTD is obtained by Eqs. (9, (10).

$$\frac{V_1-V_2}{I} = RTD + R_{L1} + R_{L2} \tag{9}$$

$$RTD = \frac{V_1-V_2}{I} - \left(R_{L1}+R_{L2}\right) \tag{10}$$

The two-wire connection is very simple, only need to introduce two wires. However, its measurement accuracy is not high because the resistance brought by the wires L_1 and L_2 is ignored during the measurement process, resulting in the resistance being counted into the RTD together with Pt100, thus affecting the measurement accuracy. Therefore, the wiring method of measurement accuracy is low, only for the lower requirements of temperature measurement accuracy, not for high-precision temperature measurement.

(2) Three-wire connection. The wiring method compared with the two-wire wiring system, and the introduction of a wire, shown in the figure for L_3. The role of the wire is to compensate for the error caused by the resistance of the wire. In order to better compensate for the resistance error, it is required that L_1, L_2, L_3 three wires work in the same environmental parameters, and has the same length, cross-sectional area and material, that is, $R_{L1} = R_{L2} = R_{L3}$. Similar to the 2-wire operation principle, the potentials V_1, V_2, V_3 are measured by applying an excitation current I to the Pt100. At the same time, L_3 is connected to a high input impedance circuit with $I_{L3} = 0$, and the resistance value of the RTD can be found from equations (11), (12), (13), and (14).

$$\frac{V_1-V_2}{I} = RTD + R_{L1} + R_{L2} \tag{11}$$

$$\frac{V_3-V_2}{I} = R_{L2} \tag{12}$$

$$R_{L1} = R_{L2} = R_{L3} \tag{13}$$

$$RTD = \frac{V_1 - V_2}{I} - 2R_{L2} = \frac{V_1 + V_2 - 2V_3}{I} \tag{14}$$

Three-wire connection method than the two-wire connection method, although high precision, but in order to reduce the measurement error, the requirements: $R_{L1} = R_{L2} = R_{L3}$, that is, the resistor material, length, cross-section is completely equal to the actual situation is difficult to do.

(3) four-wire connection. The wiring compared to the two-wire wiring method, but also at both ends of the Pt100 introduced two wires, shown in the figure for L_3, L_4. Which gives L_3, L_4 access to high input impedance circuit, at this time $I_{L3} = I_{L4} = 0$. At this time, the voltage at both ends of Pt100 can be obtained by measuring the potential difference between V_4 and V_3. Compared with the two-wire and three-wire systems, the four-wire system is directly through the potential measurement of the two ends of the Pt100 and then get the resistance value of the RTD as in equation (15). Although this wiring method is more complicated than the two-wire and three-wire systems, this method completely eliminates the resistance error caused by the wire, and therefore has a higher measurement accuracy.

$$RTD = \frac{V_4 - V_3}{I} \tag{15}$$

Based on the above analysis, this system will use a four-wire connection for Pt100 in order to realize high-precision measurement. Figure 1 is the Pt100 temperature information acquisition circuit diagram.

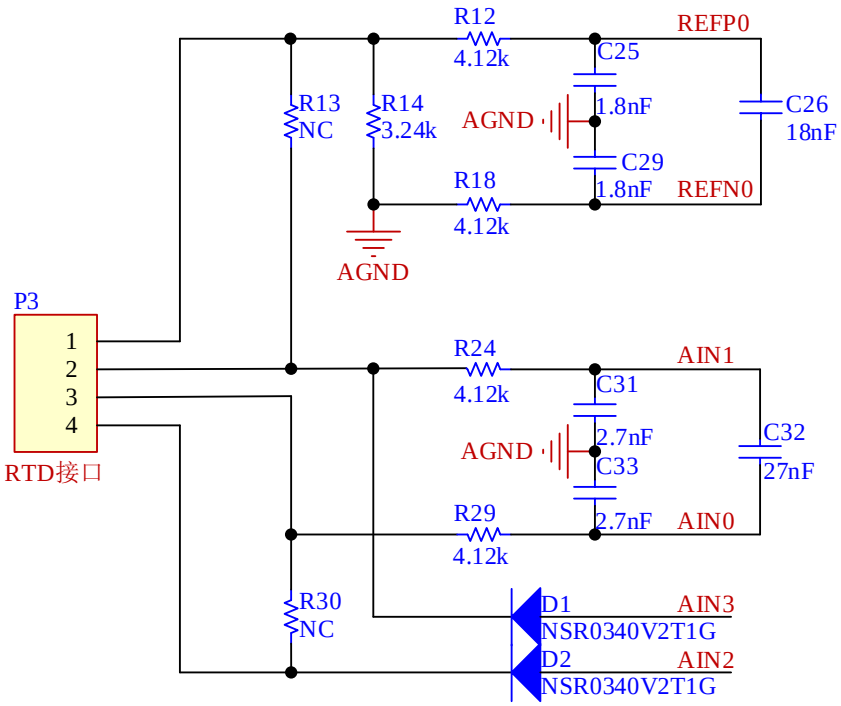

Figure 1: Temperature Information Acquisition Circuit Diagram

2.3 Inverse distance weight model for anisotropy

2.3.1 Inverse distance weighting method (IDW)

The inverse distance weighting method assumes that the influence of the observation point on the interpolated point decreases with increasing distance, i.e., an inverse relationship, with the following expression:

$$Z^* = \sum_{i=1}^{n} \left(\lambda_i Z_i \right) \tag{16}$$

where: Z^* is the predicted value; n is the number of reference sampling points selected; λ_i is the weighting coefficient of the observed point on the estimated interpolated point; Z_i is the actual value measured at the i th detection point. The weighting coefficients are given by equation (17):

$$\lambda_i = \frac{1}{d_i^b} \Bigg/ \left(\sum_{i=1}^{n} \frac{1}{d_i^b} \right) \tag{17}$$

where: d_i is the distance between the point to be interpolated and the i th observation; b is the distance attenuation coefficient.

2.3.2 Local parameter optimization inverse distance weighting method

Considering the existence of spatial heterogeneity, this paper uses a cross-validation strategy through the particle swarm optimization algorithm to optimize and preserve the local optimization results for the known reference points with parameters n and b in Eq. (17) with parameters θ and λ, respectively.

1) Particle swarm optimization algorithm

The particle swarm optimization algorithm imitates the foraging behavior of bird flocks, obtains the current group optimal value through information sharing, and iterates to get the final global optimal value, which has the advantages of good global performance and simple implementation.

When the algorithm runs, the position vector p of the particle is updated according to the best position p_{best} that it passes through and the population best position g_{best} :

$$\begin{cases} v_{id}^{k+1} = \omega v_{id}^{k} + c_1 \varphi_1 \left(p_{id}^{k} - x_{id}^{k} \right) + c_2 \varphi_2 \left(p_{gd}^{k} - x_{id}^{k} \right) \\ x_{id}^{k+1} = x_{id}^{k} + v_{id}^{k+1} \end{cases} \tag{18}$$

where: ω is the inertia coefficient; c_1 and c_2 are the learning factors, reflecting the learning ability of the particle; k represents the number of iterations; x_{id} represents the current position value in the d th dimension; p_{id} and p_{gd} represent the optimal position in the d th dimension of the particle itself and the optimal position value of the population, respectively, and φ_1 and φ_2 are uniformly distributed random numbers in the interval $[0,1]$.

2) Optimization Strategy

It is known that there are a total of N sample points $\{Z_1, Z_2, \cdots, Z_N\}$ in the study area,

and for any one of them, Z_i, the particle swarm optimization algorithm is used to find an optimal solution for the parameter $P=(n,b,\theta,\lambda)$ for optimization to obtain a set of optimal parameters P_{besti} for Z_i, as shown in equation (19):

$$\begin{aligned} P_{besti} &= \arg\min err_i(P_k)\, err_i(P_k) \\ &= \left(Z_i - Z_{Zi}^{*}(P_k)\right), i=1,2,\cdots,N \end{aligned} \tag{19}$$

where: Z_{Zi}^{*} represents the estimation without the point Z_i itself; The P_k is a certain set of parameter vectors that correspond to the coordinates of a particle; The obtained P_{besti} is the set of optimal parameters found at the point Z_i, which needs to be stored.

In order to minimize the instability caused by multi-parameter optimization, two particle populations are used in this paper for the parameter optimization process at each site: one population performs the complete optimization of $P=(n,b,\theta,\lambda)$, while the other population fixes the parameters $\theta=0$ and $\lambda=1$, i.e., only the parameters n and b are searched for optimality, and finally only the global optimal result of the most optimal population is kept.

3) Algorithm flow

The algorithm in this paper mainly contains the parameter optimization process as well as the interpolation using process, after completing the optimal parameter optimization for all known sample points, the corresponding $P_{besti}(i=1,2,\cdots,N)$ is obtained. It is assumed that the closer the spatial distance is, the more similar the values of the optimal parameters are, so for the values of the unknown points, the algorithm will use the optimal parameters of the nearest sample points for approximate optimization estimation.

Figure 2 shows the flow of the algorithm in this paper. Since the parameter optimization process of each reference point is independent of each other, concurrent optimization processing can be carried out to improve the computing speed of the program. In addition, since the algorithm needs to repeatedly calculate the distance between nodes to find the nearest reference point, in order to improve the efficiency, this paper uses K-dimensional tree (KD-Tree) to optimize the querying process, which can reduce the computation time when selecting the nearest reference point.

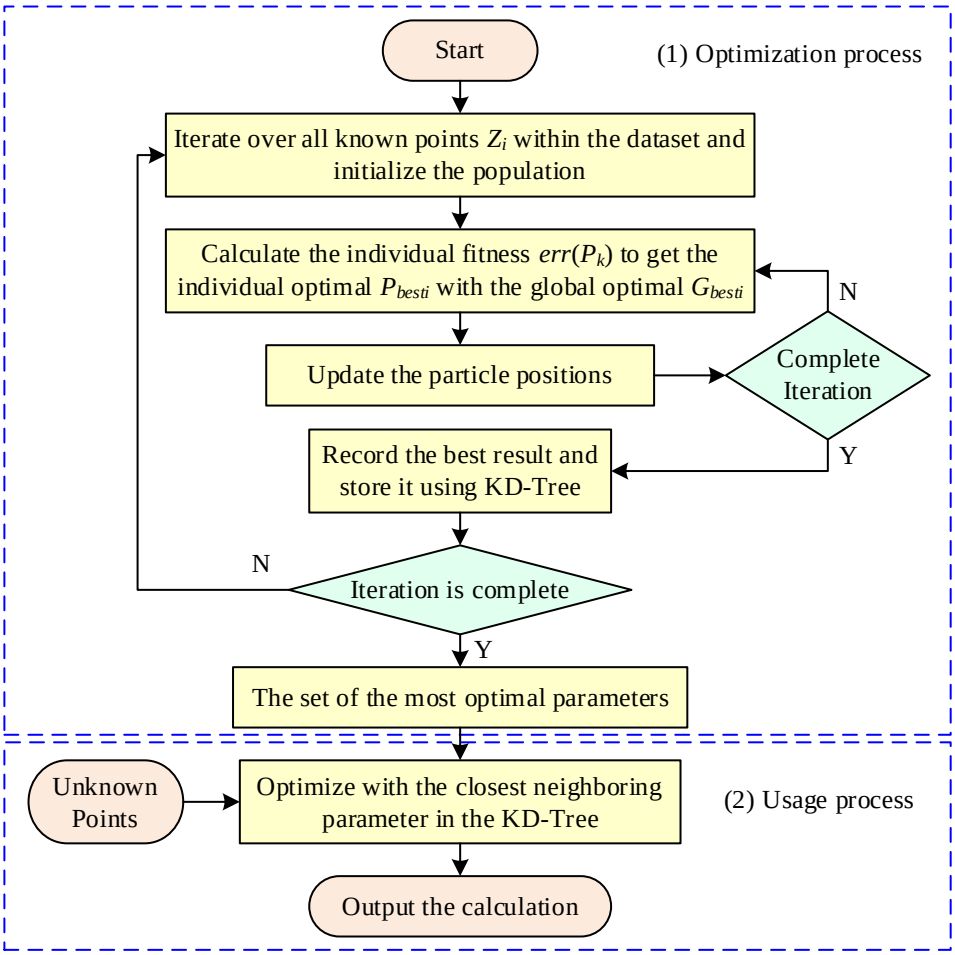

Figure 2: Flowchart of proposed algorithm

3 Temperature prediction simulation and energy saving optimization practices

In this chapter, the constructed model is applied to the temperature field prediction and energy-saving design of large buildings, and the effectiveness of the model is proved through experimental analysis.

3.1 Relationship between search distance and weighting factor

In this paper, the tall transition space of a typical comprehensive office building in the northern cold region is selected as the research object. The building is a four-story building with a total height of 18 meters, structural form of the main frame structure, local large-span glass roof for the grid structure. The atrium transition space is located in the center of the building, with an area of about 838m², and the two entrances of the building in the north and south are connected with the transition space through a passageway; the south, north and west sides are surrounded by rooms, and the east direction is attached to another building. The atrium transition space and part of the first floor are heated by radiant floor heating, and the rest of the indoor rooms are heated by radiators. The roof is a double-layer hollow LOW-E laminated glass roof with high natural light transmission rate. The transition space atrium runs from the first to the fourth floor of the building, with a total height of 20m in the interior space, of which the north and east

facing parts of the second floor are equipped with elevated platforms.

The weight coefficients in the IDW algorithm play a key influence on the interpolation results. Usually, the neighborhood search shape of interpolation adopts a circle or a square, i.e., with the point to be interpolated as the center, a circle or a square search domain with a specific radius is established, and any valid site within this search domain is taken as the sample point of this interpolation. In order to simplify the process of site traversal and calculation, this paper adopts a circular search domain, and the search radius is directly based on the latitude and longitude grid distance as a unit.

Parameter settings: the search radius R take 1-10, step 1, does not limit the maximum number of sites within the radius to participate in the interpolation; distance weight coefficients take 1-5, step 0.5, a total of 2925 times in the last 4 years, each time about 500 sites temperature data, one by one, the interpolation of the IDW algorithm calculations, and then take the arithmetic mean for the root-mean-square error for each time of each site, respectively.

Figure 3 shows the search distance versus weight coefficients. Figures 3(a) and 3(b) represent the relationship between search distance and weight coefficients for the two methods of interpolated revisions of temperature with altitude, and interpolated revisions of the relationship between the temperature field and the barometric pressure field, respectively. Each figure has five curves each, representing the relationship between different weighting coefficients and root mean square error from bottom to top for height distances of 2, 4, 6, 8, and 10, respectively. Analyzing the two plots, it can be seen that the overall trend of the two methods is nearly the same, both of which minimize the error of the interpolation results when the height distance is 2 and the weighting coefficient is 2.5-3. With the increase of the search radius, the interpolation error is getting larger and larger. Therefore, the search height distance of this paper is set to 2 and the weight coefficient is set to 2.75 to obtain the minimum interpolation error.

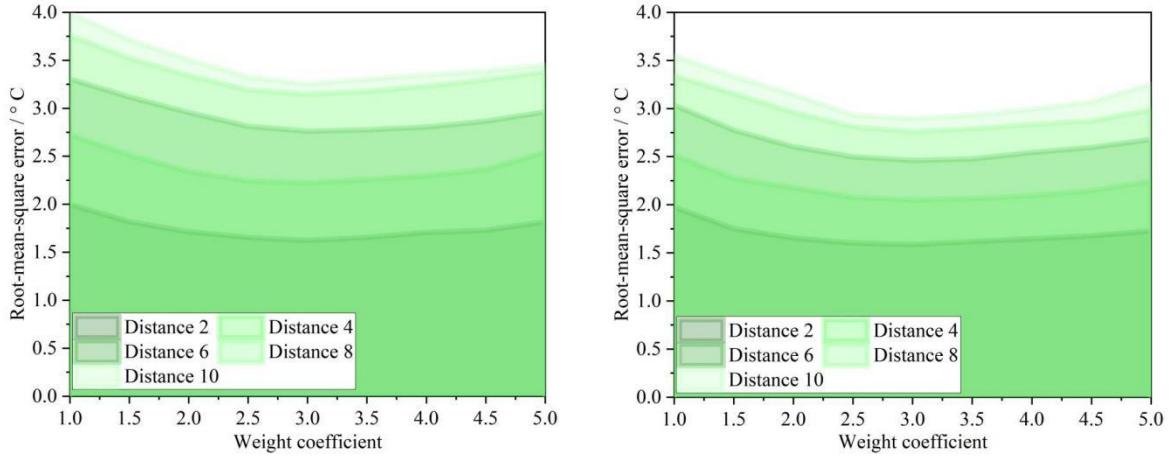

(a) Interpolation revision of temperature with height

(b) Interpolation revision of temperature field and pressure field

Figure 3: Relation between search distance and weight coefficient

3.2 Temperature difference characterization

3.2.1 Vertical Average Temperature Characteristics of the Layers

In order to compare the accuracy of the predicted values of the temperature field, it is necessary to first collect the actual average temperature distribution characteristics of the temperature field through measurements. In this section, the characteristics of the temperature difference in the vertical and horizontal directions of the tall transition space of this building are used as an

example to analyze the average temperature characteristics in each direction of the tall transition space of this building.

Table 1 demonstrates the average temperature distribution characteristics of the atrium transition space of this building in the vertical direction at each level. It is found that no matter in sunny or non-sunny weather, the overall temperature of the first floor of the nine groups of measurement points is the highest, and the overall temperature of the fourth floor is the lowest, and the difference between the two averages in sunny weather is 0.62℃, and the difference between the two averages in non-sunny weather is 1.02℃, so that the distribution of the temperature gradient in non-sunny weather is more obvious than that in sunny weather. Considering the precision of the testing instrument, the average temperature of the second and third layers can be approximated as no difference, without obvious gradient distribution characteristics, indicating that the transition space in the vertical direction of the central space temperature change is not obvious, showing a more stable state. The average temperature difference between the first layer and the second (third) layer in the vertical direction is about 0.58℃, about 0.45℃ in sunny weather, and about 0.71℃ in non-sunny weather. This indicates that the temperature distribution is mainly reflected in the part of the transition space close to the working area, and the trend of change with the increase of the number of layers tends to stabilize gradually. As the number of layers rises, the average temperature difference between the layers on sunny and non-sunny days shows a decreasing trend.

Table 1: Average temperature characteristics of each layer in vertical direction

Temperature	Average vertical temperature on Clear days (°C)				Average vertical temperature on non-clear days (°C)			
Number of floors	Layer 1	Layer 2	Layer 3	Layer 4	Layer 1	Layer 2	Layer 3	Layer 4
Test point 1 group	14.43	13.87	13.80	13.30	15.02	14.34	14.15	13.82
Test point 2 group	14.33	13.95	14.04	13.74	14.94	14.46	14.43	14.20
Test point 3 group	14.43	14.19	13.99	13.97	15.00	14.39	14.49	14.27
Test point 4 group	14.44	14.58	14.28	14.12	16.03	15.07	14.78	14.35
Test point 5 group	15.68	14.39	13.91	14.39	16.26	14.86	14.40	14.51
Test point 6 group	14.34	14.10	15.06	13.78	14.98	14.51	15.49	14.35
Test point 7 group	14.50	14.18	13.97	13.88	15.11	14.68	14.33	14.35
Test point 8 group	14.52	14.02	14.10	14.27	15.09	14.51	14.61	14.44
Test point 9 group	14.57	13.89	13.91	14.19	15.17	14.37	14.41	14.17
Mean value	14.58	14.13	14.12	13.96	15.29	14.58	14.57	14.27

3.2.2 Basic information on temperature differences between measurement points in the horizontal direction

Horizontal temperature difference characterization is generally divided into two ways: one is in the transverse plane (X-axis) and longitudinal plane (Y-axis) in two directions to study the characteristics of the temperature difference between measurement points, the other is to study the characteristics of the temperature difference between each measurement point and the adjacent measurement points. The basic idea of numerical heat transfer is to replace the original continuous field of physical quantities in time and space coordinates with a collection of values at a finite number of discrete points. When solved numerically, the partition becomes a region of finite size, which is the process of discretization. Based on the principles of numerical heat transfer calculations, the second type of temperature difference analysis is chosen in this section. The transition space work area of the selected building has a total of 16 measurement points, in

the X-axis and Y-axis direction, measurement point 1, measurement point 4, measurement point 13 and measurement point 16 have two neighboring measurement points, that is, there are two sets of temperature difference data; measurement point 2, measurement point 3, measurement point 5, measurement point 8, measurement point 9, measurement point 12, measurement point 14 and measurement point 15 have three adjacent measurement points, that is, there are three sets of Temperature difference data; in the center of the work area, measuring point 6, measuring point 7, measuring point 10 and measuring point 11 have four adjacent measuring points, that is, there are four sets of temperature difference data.

Table 2 demonstrates the results of the preliminary analysis of the temperature difference between each measurement point and its neighboring measurement points. The temperature differences at each point do not show a directional gradient consistent with the overall temperature distribution and are relatively random. The extreme value of the average temperature difference between points is 0.49°C between point 8 and point 12, and the extreme value of the average temperature difference is 0.0004°C between point 15 and point 14. Overall, the temperature difference between measurement points in the horizontal direction does not exceed 0.5°C, which is in line with the actual situation.

Table 2: Basic information of temperature difference between measuring points

Temperature difference	Average temperature difference (℃)	Maximum (° C)	Minimum (° C)	Extreme difference (℃)	Temperature difference	Average temperature difference (℃)	Maximum (° C)	Minimum (° C)	Extreme difference (℃)
1-2	0.17	0.37	-0.27	0.68	7-11	0.16	0.58	-0.11	0.66
1-5	0.19	0.45	-0.16	0.68	8-12	**0.49**	0.79	0.08	0.67
3-2	0.05	0.34	-0.31	0.66	10-9	0.21	0.58	0.32	0.55
6-2	0.14	0.28	-0.10	0.45	13-9	0.18	1.06	-0.11	1.13
4-3	0.18	0.36	-0.25	0.61	10-11	0.07	0.28	-0.12	0.47
3-7	0.13	0.41	-0.24	0.64	14-10	0.03	0.28	-0.27	0.59
8-4	0.05	0.12	-0.27	0.47	11-12	0.09	0.17	-0.17	0.39
6-5	0.11	0.46	-0.13	0.54	15-11	0.17	0.28	-0.18	0.46
5-9	0.36	0.71	0.32	0.77	12-16	0.16	0.53	-0.06	0.57
6-7	0.20	0.46	-0.15	0.53	14-13	0.05	0.17	-0.97	1.14
6-10	0.26	0.74	0.15	0.78	15-14	**0.0004**	0.28	-0.25	0.57
8-7	0.27	0.54	0.17	0.51	15-16	0.39	0.53	0.02	0.54

3.3 Simulation results of case building temperature distribution and verification of real measurements

3.3.1 Comparison of Simulated and Measured Horizontal Mean Temperature Values

In order to verify the reliability of the temperature prediction of the algorithmic model in this paper, the values of the temperature distribution simulated by the model are analyzed in comparison with the measured values of the temperature distribution in the atrium transition space. The comparative analysis is divided into two parts: horizontal temperature distribution and vertical temperature distribution. Figure 4 shows the comparison between the simulated and measured values of the horizontal temperature. As can be seen from the comparison between the measured and simulated values in Figure 4, the simulated temperature values have a certain error due to a certain gap between the simulated parameters and the actual situation, in which the three measurement points located in the southwest direction of the atrium transition space (measurement points 1, 2, and 10) cannot be accurately set due to the distance from the building envelope, which results in a greater influence of the group of measurement points by the outdoor meteorological parameters, so the actual value is slightly lower than the measured

value. The actual value is slightly lower than the measured value. On the whole, the maximum value of the temperature difference is 0.822℃, and the average value of the temperature difference is about 0.250℃, so the trend of the model's horizontal temperature distribution prediction simulation value matches the measured value to a high degree.

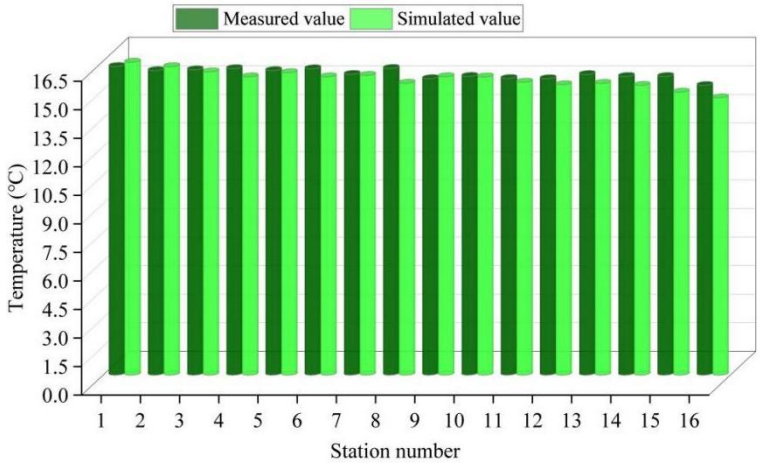

Figure 4: Comparison between simulated and measured horizontal temperature values

3.3.2 Comparison of Simulated and Measured Vertical Mean Temperature Values

In the vertical direction, in order to make the comparative results more concisely expressed, the average values of the temperatures of each floor in the simulation results were selected to be compared with the measured temperature values. Figure 5 shows the comparison between the simulated and measured values of the vertical temperature distribution in the atrium transition space of the selected building on November 28, 2020 at 13:00 noon. As can be seen from the results of the comparison between the measured and simulated values in Fig. 5, as a whole, the maximum value of the temperature difference is 0.216°C, and the average value of the temperature difference is about 0.162°C, with a small average error, and the trend of the simulated values of the vertical temperature distribution agrees with the measured values to a very high degree. It shows that the model in this paper has good reliability of prediction data and can be used in the subsequent energy saving analysis of building temperature field.

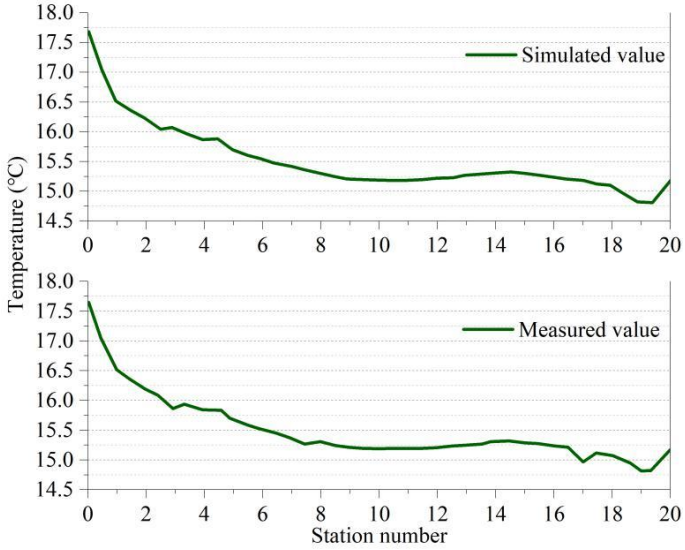

Figure 5: Comparison of simulated and measured vertical temperature distribution

3.4 Analysis of energy consumption optimization results

Based on the predicted temperature results, the optimization of building temperature field cold loads is carried out through the model to achieve the goal of energy saving and emission reduction. The EnergyPlus software, a commonly used digital energy-saving design in the market, is selected as a comparison, and 10 energy consumption simulations are conducted for the optimization of multiple temperature field cold loads inside the building under the conditions of the same environment, the same equipment applicability, and the same thermal parameter of the enclosure structure. Table 3 shows the comparative analysis of the energy consumption simulation results of this paper's model and EnergyPlus software. From the data analysis in Table 3, it can be found that the solutions given by this paper's model in all 10 energy simulations have less amount of energy consumption. Especially in the 8th energy consumption simulation, the energy consumption scheme of this paper's model is able to achieve the optimization of the building energy consumption of 0.80kWh per square meter relative to the energy-saving design scheme of EnergyPlus software. Even in the 5th energy consumption simulation, the model of this paper can at least achieve the optimization of building energy consumption of 0.08kWh per square meter. Based on the simulation results, it can be judged that the model in this paper can effectively achieve the temperature field temperature prediction in the energy-saving design of the building and give a reasonable energy consumption optimization scheme.

Table 3: Comparative analysis of energy consumption simulation results

Serial number	Predicted energy consumption(kWh/m²)		Energy consumption reduction(kWh/m²)
	Textual model	EnergyPlus software	
1	52.02	52.54	0.52
2	44.10	44.58	0.48
3	65.11	65.28	0.17
4	41.98	42.60	0.62
5	68.40	68.32	0.08
6	60.75	61.14	0.39
7	58.51	59.15	0.64
8	68.17	68.97	0.80
9	58.05	58.36	0.31
10	54.42	54.62	0.20

4 Conclusion

This paper constructs an accurate prediction and energy-saving optimization model of building temperature field based on IDW algorithm to provide technical support for building energy-saving design. The mean values of the horizontal and vertical temperature difference of the model are 0.250℃ and 0.162℃ respectively, which have a small temperature difference. 10 groups of energy consumption simulation, the energy saving of the model in this paper reaches 0.80kWh/m² at the highest, and the lowest is also 0.08kWh/m², which verifies the validity of energy-saving scheme. From the study of this paper, it can be known that the model of IDW algorithm has significant advantages in the analysis of vertical and horizontal temperature difference characteristics and optimization of energy consumption. In the future, in-depth research can be carried out on how to introduce a real-time adaptive calibration mechanism in

the model to realize the automated adjustment of the optimal parameters, so as to improve the model's ability to cope with the complex and variable meteorological conditions, and to ensure the effect of building energy-saving optimization.

References

[1] Huang, H., Wang, H., Hu, Y. J., Li, C., & Wang, X. (2022). The development trends of existing building energy conservation and emission reduction—A comprehensive review. *Energy Reports*, 8, 13170-13188.

[2] Yuan, X., Zhang, X., Liang, J., Wang, Q., & Zuo, J. (2017). The development of building energy conservation in China: A review and critical assessment from the perspective of policy and institutional system. *Sustainability*, 9(9), 1654.

[3] Zhao, X. G., & Gao, C. P. (2022). Research on Energy-Saving Design Method of Green Building Based on BIM Technology. *Scientific Programming*, 2022(1), 2108781.

[4] Lamsal, P., Bajracharya, S. B., & Rijal, H. B. (2023). A review on adaptive thermal comfort of office building for energy-saving building design. *Energies*, 16(3), 1524.

[5] Teng, J., Wang, P., Mu, X., & Wang, W. (2021). Energy-saving performance analysis of green technology implications for decision-makers of multi-story buildings. *Environment, Development and Sustainability*, 23, 15639-15665.

[6] Zhang, K. (2020). Energy-saving parameterized design of buildings based on genetic algorithm. *International Journal of Building Pathology and Adaptation*, 38(5), 785-795.

[7] Pioppi, B., Piselli, C., Crisanti, C., & Pisello, A. L. (2020). Human-centric green building design: the energy saving potential of occupants' behaviour enhancement in the office environment. *Journal of Building Performance Simulation*, 13(6), 621-644.

[8] Rijal, H. B., Yoshida, K., Humphreys, M. A., & Nicol, J. F. (2021). Development of an adaptive thermal comfort model for energy-saving building design in Japan. *Architectural Science Review*, 64(1-2), 109-122.

[9] Kwasnowski, P., Fedorczak-Cisak, M., & Knap, K. (2017, October). Problems of technology of energy-saving buildings and their impact on energy efficiency in buildings. *In IOP Conference Series: Materials Science and Engineering* (Vol. 245, No. 7, p. 072043). IOP Publishing.

[10] Chen, H., Shen, G. Q., Feng, Z., & Liu, Y. (2024). Optimization of energy-saving retrofit solutions for existing buildings: A multidimensional data fusion approach. *Renewable and Sustainable Energy Reviews*, 201, 114630.

[11] Tu, D., Tang, J., Zhang, Z., & Sun, H. (2023). Thermal environment optimization in a large space building for energy-saving. *Case Studies in Thermal Engineering*, 51, 103649.

[12] Li, K., Zheng, W., Xue, W., & Wang, Z. (2023). Fast reconstruction of indoor temperature field for large-space building based on limited sensors: An experimental study. *Energy and Buildings*, 298, 113493.

[13] Wang, X., Zhao, J., Wang, F., Song, B., & Zhang, Q. (2021). Air supply parameter optimization of a custom nonuniform temperature field based on the POD method. *Building and Environment*, 206, 108328.

[14] Li, Q., Zhang, L., Zhang, L., & Wu, X. (2021). Optimizing energy efficiency and thermal comfort in building green retrofit. *Energy*, 237, 121509.

[15] Zhang, S., Cheng, Y., Fang, Z., Huan, C., & Lin, Z. (2017). Optimization of room air temperature in stratum-ventilated rooms for both thermal comfort and energy saving. *Applied Energy*, 204, 420-431.